

EFFECT OF BEAM CHROMATICITY ON FOREGROUNDS IN WIDE-FIELD MEASUREMENTS OF REDSHIFTED 21 CM POWER SPECTRA

NITHYANANDAN THYAGARAJAN^{1*}, TBD

Draft version February 8, 2016

ABSTRACT

Keywords: cosmology: observations — dark ages, reionization, first stars — large-scale structure of universe — methods: statistical — radio continuum: galaxies — techniques: interferometric

1. INTRODUCTION

The period in the history of the Universe characterized by the transition of neutral hydrogen in the intergalactic medium (IGM) to a fully ionized state due to the formation of radiating objects such as the first stars and galaxies is referred to as the Epoch of Reionization (EoR). This is an important period of nonlinear growth of matter density perturbations and astrophysical evolution leading to the large scale structure observed currently in the Universe. And yet, this period in the Universe’s history has remained poorly probed to date with observations.

The redshifted neutral hydrogen from the IGM in this epoch has been identified to be one of the most promising and direct probes of the EoR (Sunyaev & Zeldovich 1972; Scott & Rees 1990; Madau et al. 1997; Tozzi et al. 2000; Iliev et al. 2002). Numerous experiments using low frequency radio telescopes targeting the redshifted 21 cm line from the spin-flip transition of HI have become operational such as the Murchison Widefield Array (MWA; Lonsdale et al. 2009; Bowman et al. 2013; Tingay et al. 2013), the Precision Array for Probing the Epoch of Reionization (PAPER; Parsons et al. 2010), the Low Frequency Array (LOFAR; van Haarlem et al. 2013) and the Giant Metrewave Radio Telescope EoR experiment (GMRT; Paciga et al. 2013). These instruments have sufficient sensitivity for a statistical detection of the EoR signal via estimating the spatial power spectrum of the redshifted HI temperature fluctuations (Beardsley et al. 2013; Thyagarajan et al. 2013). These instruments are intended to be precursors and pathfinders to the next generation of low frequency radio observatories such as the Hydrogen Epoch of Reionization Array³ (HERA; DeBoer et al. 2015) and the Square Kilometre Array⁴ (SKA). These next-generation instruments will advance the capability from a mere statistical detection of the signal to a direct three-dimensional tomographic imaging of the HI during the EoR.

The most significant challenge to low frequency EoR observations arises from the extremely bright Galactic and extragalactic foreground synchrotron emission which are $\sim 10^4$ times stronger than the desired EoR signal (Di Matteo et al. 2002; Ali et al. 2008; Bernardi et al. 2009, 2010; Ghosh et al. 2012). All the current and future

instruments rely on the inherent differences in spatial isotropy and spectral smoothness between the EoR signal and the foregrounds to extract the EoR power spectrum (see, e.g., Furlanetto & Briggs 2004; Morales & Hewitt 2004; Zaldarriaga et al. 2004; Santos et al. 2005; Furlanetto et al. 2006; McQuinn et al. 2006; Morales et al. 2006; Wang et al. 2006; Gleser et al. 2008).

When expressed in the coordinate system of power spectrum measurements described by the three-dimensional wavenumber (k), the foreground emission is restricted to a wedge-shaped region commonly referred to as the *foreground wedge* (Bowman et al. 2009; Liu et al. 2009, 2014a,b; Datta et al. 2010; Liu & Tegmark 2011; Ghosh et al. 2012; Morales et al. 2012; Parsons et al. 2012b; Trott et al. 2012; Vedantham et al. 2012; Dillon et al. 2013; Pober et al. 2013; Thyagarajan et al. 2013; Dillon et al. 2014) whereas the EoR signal has spherical symmetry due to its isotropy which appears elongated along line of sight k modes due to peculiar velocity effects when dominated by matter density perturbations during early stages of reionization.

The extreme dynamic range required to subtract foregrounds precisely demands high precision modeling of foregrounds as observed by modern wide-field instruments (Thyagarajan et al. 2015b,a). Their studies of effects of wide-field measurements of EoR power spectra have demonstrated the *pitchfork* effect wherein foreshortening of baselines causes a prominent enhancement of foreground power near the horizon limits of the *foreground wedge* as well in the contamination beyond. In this paper, we explore yet another phenomenon that inherently extends foreground power beyond the *wedge*, namely, that arising from the chromaticity of the antenna power pattern.

This paper is organized as follows. §2 introduces the HERA instrument. A brief summary of the delay spectrum technique used extensively in this analysis and the recently confirmed *pitchfork* effect are presented in §3. §4 describes foreground simulations including antenna beam pattern and all-sky foreground models. §5 investigates the effects of chromaticity of antenna beam on the resulting delay power spectrum and the cosmologically motivated constraints it places on dish reflectometry. Our findings are summarized in §6.

2. THE HYDROGEN EPOCH OF REIONIZATION ARRAY DeBoer et al.(2016)

3. DELAY SPECTRUM

¹ Arizona State University, School of Earth and Space Exploration, Tempe, AZ 85287, USA

* e-mail: t_nithyanandan@asu.edu

³ <http://reionization.org/>

⁴ <https://www.skatelescope.org/>

A brief description of the delay spectrum technique (Parsons et al. 2012a,b) is provided here. We borrow the notation used in Thyagarajan et al. (2015b).

Visibilities measured by an interferometer are given by (van Cittert 1934; Zernike 1938; Thompson et al. 2001):

$$V_b(f) = \iint_{\text{sky}} A(\hat{s}, f) I(\hat{s}, f) e^{-i2\pi f \frac{\mathbf{b} \cdot \hat{s}}{c}} d\Omega, \quad (1)$$

where, \mathbf{b} is the vector joining antenna pairs (commonly referred to as the baseline vector), \hat{s} is the unit vector denoting direction on the sky, f denotes frequency, c is the speed of light, $d\Omega$ is the solid angle element to which \hat{s} is the unit normal vector, $I(\hat{s}, f)$ and $A(\hat{s}, f)$ are the sky brightness and antenna's directional power pattern, respectively, as a function of \hat{s} and f . The *delay spectrum*, $\tilde{V}_b(\tau)$, is defined as the inverse Fourier transform of $V_b(f)$ along the frequency coordinate:

$$\tilde{V}_b(\tau) \equiv \int V_b(f) W(f) e^{i2\pi f \tau} df, \quad (2)$$

where, $W(f)$ is a spectral weighting function which can be chosen to control the quality of the delay spectrum (Vedantham et al. 2012; Thyagarajan et al. 2013), and τ represents the signal delay between antenna pairs:

$$\tau = \frac{\mathbf{b} \cdot \hat{s}}{c}. \quad (3)$$

The delay spectrum has a close resemblance to cosmological H I spatial power spectrum. Thus, the delay power spectrum is defined as:

$$P_d(\mathbf{k}_\perp, k_\parallel) \equiv |\tilde{V}_b(\tau)|^2 \left(\frac{1}{\Omega \Delta B} \right) \left(\frac{D^2 \Delta D}{\Delta B} \right) \left(\frac{\lambda^2}{2k_B} \right)^2, \quad (4)$$

with

$$\mathbf{k}_\perp \equiv \frac{2\pi(\frac{\mathbf{b}}{\lambda})}{D}, \quad (5)$$

$$k_\parallel \equiv \frac{2\pi\tau f_{21} H_0 E(z)}{c(1+z)^2}, \quad (6)$$

where, ΔB is the bandwidth, λ is the wavelength of the band center, k_B is the Boltzmann constant, f_{21} is the rest frame frequency of the 21 cm spin flip transition of H I, z is the redshift, $D \equiv D(z)$ is the transverse comoving distance, ΔD is the comoving depth along the line of sight corresponding to ΔB , and h , H_0 and $E(z) \equiv [\Omega_M(1+z)^3 + \Omega_k(1+z)^2 + \Omega_\Lambda]^{1/2}$ are standard terms in cosmology, and following Parsons et al. (2014),

$$\Omega \Delta B = \iint |A(\hat{s}, f) W(f)|^2 d\Omega df. \quad (7)$$

In this paper, we use $\Omega_M = 0.27$, $\Omega_\Lambda = 0.73$, $\Omega_K = 1 - \Omega_M - \Omega_\Lambda$, $H_0 = 100 \text{ km s}^{-1} \text{ Mpc}^{-1}$, and $P_d(\mathbf{k}_\perp, k_\parallel)$ is in units of $\text{K}^2 (h^{-1} \text{ Mpc})^3$.

It was recently discovered that in wide-field measurements diffuse foreground emission from wide off-axis angles appear enhanced in the delay spectrum near the edges of the *foreground wedge* even on wide antenna spacings (Thyagarajan et al. 2015b). Called the *pitchfork*

effect, this arises due to severe foreshortening of baseline vectors towards the horizon along joining the antenna pairs thereby enhancing their sensitivity to large scale structures in these directions. Since delay spectrum maps directions on the sky to delay bins, the emission from large scales near the horizon appears enhanced in delay bins near the horizon limits of the *foreground wedge*. Since these delay modes lie adjacent to those considered sensitive to the EoR signal, they cause a significant contamination of line-of-sight modes critical for EoR signal detection. These findings were confirmed in MWA observations (Thyagarajan et al. 2015a).

It was also demonstrated in these studies that design of antenna power pattern, specifically its amplitude near the horizon, is an important tool in mitigating foreground contamination caused by these wide-field effects. A dish characterized by a nominal *Airy* pattern was found to mitigate this contamination by over four and two orders of magnitude relative to a dipole and a phased array of dipoles respectively. HERA has significantly based its antenna design principles on these findings in choosing its antenna geometry while paying close attention to the properties of the resulting antenna power pattern.

In this paper, we investigate the spectral properties of the proposed dish design through their effects on the resultant foreground delay power spectrum and the constraints they place on attenuation required to suppress reflections between the dish-receiver assembly to within tolerable limits.

4. SIMULATIONS

We simulate wide-field visibilities for 19-element HERA from all-sky antenna power pattern and foreground models using the PRISim⁵ software package. The simulations cover 24 hr of observation in *drift* mode consisting of 80 accumulations spanning 1080 s each. The total bandwidth is 100 MHz centered on 150 MHz consisting of 256 channels with 390.625 kHz frequency resolution. Models of the antenna power pattern and foregrounds are described below.

4.1. Antenna Power Pattern

The High Frequency Structural Simulator (HFSS) was used to model the dish and its angular response used in this study. The HFSS model used prime focus optics with a 14 m faceted parabola with a spar f/D ratio of 0.32. The model has a 1 m central hole in the aluminum surface which is filled with a dielectric material similar to dry soil. The feed used a full PAPER dipole inside of a cylindrical backplane, the backplane is modeled as an aluminum surface. For the metal parts of the dipole, the discs were modeled as aluminum at the actual size, and the arms and terminals were modeled as copper. Dielectric stand-offs and supporting members were included. For the calculations, one pair of arms was excited using a modal port. These models cover a frequency range of 100–200 MHz in intervals of 1 MHz. Refer to DeBoer et al. (2016) for a complete description of the dish model.

⁵ The Precision Radio Interferometry Simulator (PRISim) is publicly available at <https://github.com/nithyanandan/PRISim>

For reference, we use two other models for the antenna power pattern. The first is a nominal *Airy* pattern corresponding to a uniformly illuminated circular aperture of 14 m diameter and the second is an achromatic model where the response of the design at 150 MHz of the HFSS model described above was fixed as the hypothetical response at all frequencies covering the entire band. This frequency independent model will be used to isolate the effects of spectral structures in the antenna power pattern (or beam chromaticity) on foreground delay power spectra.

In a related series of papers, Neben et al. (2016; submitted) discuss the agreement of these model antenna beam patterns with actual measurements and Ewall-Wice et al. (2016; submitted) model the reflections and return loss expected in the proposed antenna-receiver assembly. Our focus in this paper is to investigate chromaticity of antenna power patterns from the point of view of their impact on foreground contamination in delay power spectra.

4.2. Foreground Model

Our all-sky foreground model is the same as the one in Thyagarajan et al. (2015b). It consists of diffuse emission (de Oliveira-Costa et al. 2008) and point sources. The latter is obtained from a combination of the NRAO VLA Sky Survey (NVSS; Condon et al. 1998) at 1.4 GHz and the Sydney University Molonglo Sky Survey (SUMSS; Bock et al. 1999; Mauch et al. 2003) at 843 MHz with a mean spectral index of -0.83. The diffuse sky model has an angular resolution of 13.74 and a spectral index estimated for every pixel.

4.3. EoR Model

For reference, we use two models of EoR. In the first, simulations of the HI signal were created using the publicly available 21cmFAST⁶ code described in Mesinger et al. (2011). The code uses the excursion set formalism of Furlanetto et al. (2004) to generate ionization and 21cm brightness fields for numerous redshifts. The model shown in this paper assumes the same fiducial values of $T_{\text{vir}}^{\text{min}} = 2 \times 10^4$ K (virial temperature of minimum mass of dark matter halos that host ionizing sources), $\zeta = 20$ (ionization efficiency), and $R_{\text{mfp}} = 15$ Mpc (mean free path of UV photons) which predicts the redshift of 50% ionization (and hence a peak in the power spectrum signal) to be at $z = 8.5$ as in Ewall-Wice et al. (2016; submitted). The second model is borrowed from the simulations described in detail in Lidz et al. (2008). Hereafter, we refer to these two as EoR models 1 and 2 respectively.

5. CHROMATICITY OF POWER PATTERN

The equation for delay spectrum describes the mapping between sky location of a foreground object and delay. The chromatic nature (variation with frequency) of the antenna power pattern results in a convolution of the geometrical mapping with the delay response of spectral chromaticity of the power pattern. This can result in a significant spillover of foreground power beyond the horizon delay limits especially in the case of foregrounds near the horizon.

⁶ http://homepage.sns.it/mesinger/DexM_21cmFAST.html

5.1. Directional Chromaticity of Power Pattern

Fig. 1 demonstrates the beyond-the-horizon spillover even from a flat-spectrum point source at different off-axis angles. The three panels correspond to delay spectra from different positions of the point source – 0° (left), 45° (middle) and 89° (right) – from the zenith. The phase centers are located at the source positions and hence the delay spectra are centered on $\tau = 0$ ns. The response of the simulated dish power pattern (dashed line) is compared with that from an *Airy* pattern resulting from a nominal uniformly illuminated circular disk (solid line). The gray vertical lines correspond to the horizon limits at ± 48.7 ns for a 14.6 m antenna spacing. In all these cases, a *Blackman-Harris* window function has been applied along the spectral axis.

At 0° off-axis, the *Airy* pattern has no spectral variation except that introduced by the *Blackman-Harris* window function and thus reproduces its Fourier response centered at $\tau = 0$ ns whereas the simulated power pattern is found to exhibit some spectral variation giving rise to the wings on either side of $\tau = 0$ ns. As off-axis angle increases to 45°, both the power patterns clearly exhibit chromaticity. The simulated pattern not only has a higher magnitude inside the horizon limits (by a factor ~ 10) but also exhibits higher chromaticity (by many orders of magnitude) in modes beyond the horizon relative to that of an *Airy* pattern. In contrast, at 89° off-axis, not only does the simulated pattern have higher chromaticity in high delay modes but is also two orders of magnitude higher in amplitude inside the horizon limits relative to the nominal *Airy* pattern.

It is important to note that in a generic scenario where visibilities are not phased to a specific foreground location, the chromaticity of the power pattern will imprint itself on location of the foreground objects in delay space and will give rise to significant spillover especially from foregrounds near the horizon.

We generalize the analysis above by computing the delay power spectrum of the power pattern along its spectral axis in every direction in an effort to study its performance as a function of angle on the sky.

$$A'(l, m, \tau) = \int A(l, m, f) e^{-j2\pi f\tau} df \quad (8)$$

We define the directional chromaticity of antenna power pattern as:

$$C(l, m) = \frac{\int_{|\tau| > 60 \text{ ns}} |A'|^2 d\tau}{\int_{|\tau| > 60 \text{ ns}} d\tau} \quad (9)$$

where, the limit $|\tau| > 60$ ns was chosen to represent a region well beyond the horizon limits (± 48.7 ns) for a 14.6 m antenna spacing. It thus measures the average power arising out of chromaticity in each delay mode beyond $|\tau| > 60$ ns.

Fig. 2 shows the directional chromaticity, $C(l, m)$, of the power patterns of an *Airy* disk for reference (left) and a simulated disk (middle) on an orthographic projection onto direction cosines. Their color scale is shown at the top for reference. The chromaticity of the *Airy* pattern is symmetric and always below 500. On the other hand, a simulated disk exhibits higher levels of chromaticity in

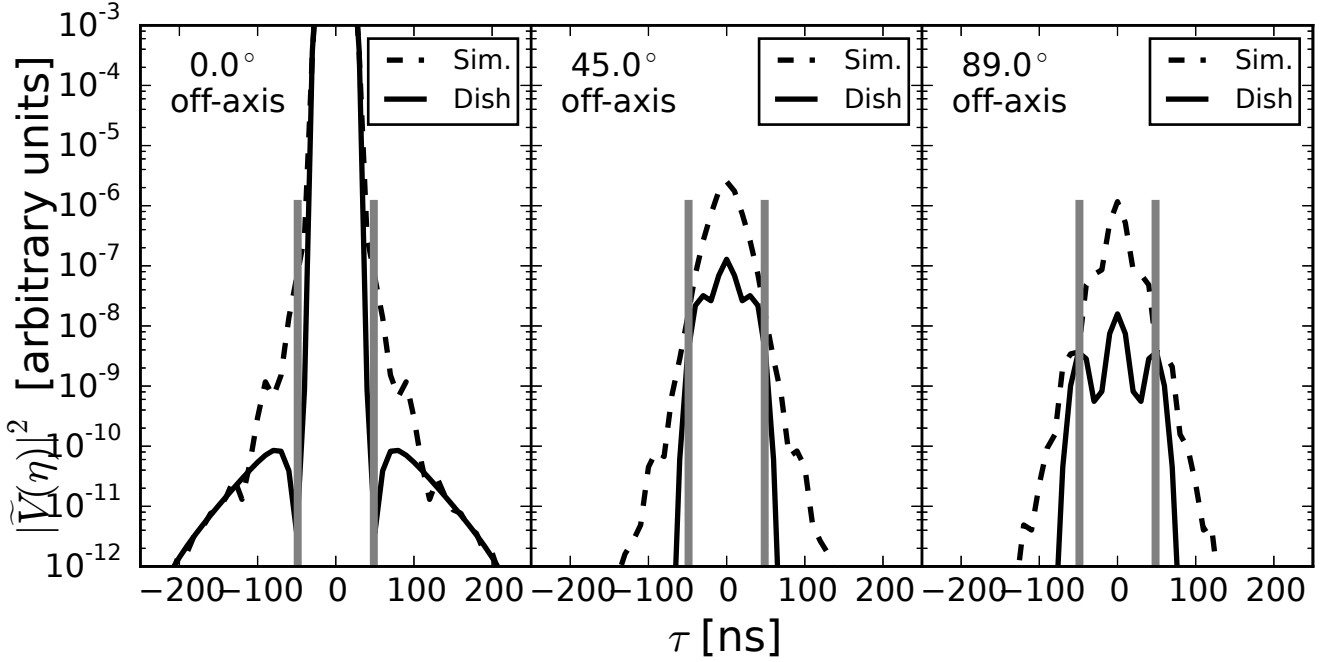


Figure 1. Chromaticity of antenna power pattern at directions off-axis.

the range 100–50,000. The ratio of their chromaticities is shown on the right with corresponding color scale on its right. The simulated disk is more chromatic than the nominal *Airy* disk only by factors $\lesssim 4$. Thus the simulated disk for HERA achieves reasonable control on the chromaticity near the horizon despite the very high levels near the center.

Also shown are the tracks (black dots) of point sources brighter than 50 Jy in the LST range 0–12 hrs. The solid circle near the bottom denotes the south celestial pole. It is noted that there are a few bright point sources that spend a majority of time in this LST range near the northern and southern horizons which will contaminate the measured visibilities on north-south antenna spacings. Simulations of the antenna power pattern must take the bright foreground locations, especially near the horizon, into account.

5.2. Effect on Delay Power Spectrum

Now we consider the effect of chromaticity of the power pattern on the delay power spectrum.

In HERA-19 array layout configuration, there are 30 unique baseline vectors and 8 unique baseline lengths. Fig. 3 shows the delay power spectra of foregrounds on the 8 unique baseline lengths obtained with the aforementioned models for power pattern. In all these panels, the full-band foreground delay power spectra obtained with achromatic, *Airy* and chromatic beam patterns are shown in black, red, and blue respectively. The vertical dotted lines denote the horizon limits for baseline lengths indicated in each panel. A clear trend of broadening of spillover-wings outside the horizon lim-

its is seen with increasing chromaticity. For instance, the spillover from foreground delay power spectrum obtained with chromatic beam pattern is restricted to $|k_{\parallel}| \lesssim 0.2 h \text{ Mpc}^{-1}$, with the *Airy* pattern it is restricted to $|k_{\parallel}| \lesssim 0.15 h \text{ Mpc}^{-1}$, while with the achromatic beam it is restricted to $|k_{\parallel}| \lesssim 0.12 h \text{ Mpc}^{-1}$ even on longest baseline lengths. Thus an increase in chromaticity extends the foreground spillover into higher k_{\parallel} -modes making them inaccessible for EoR HI signal detection.

Hence it is clearly demonstrated that higher the beam chromaticity, the farther the foreground contamination inherently extends beyond the horizon limits of the *foreground wedge*. The *Airy* pattern typically creates one secondary peak whereas the chromatic beam is found to produce multiple secondary peaks outside the *foreground wedge* on each side.

It must be emphasized that such a significant spillover is not limited by the horizon limits of the *foreground wedge* because this is caused by spectral structure in the antenna beam pattern in addition to that caused by position-dependent geometric phase in the visibility spectra. As a result delay-based complex deconvolution techniques such as CLEAN (Taylor et al. 1999; Parsons & Backer 2009; Parsons et al. 2012b) that rely on smoothness of foreground spectra and only spectral window shape will not have adequate information to accurately deconvolve intrinsic supra-horizon spillover arising from the chromaticity of the antenna beam. Thus, we leave delay power spectrum estimation using *foreground removal* strategy to future work and use *foreground avoidance* approach in this study.

We investigate the effect of chromaticity of power pattern in a *foreground avoidance* strategy that avoids the aforementioned deconvolution of delay spectrum. Application of window functions with high sidelobe suppression have been discussed for mitigating foreground contamination (Thyagarajan et al. 2013). In line with the

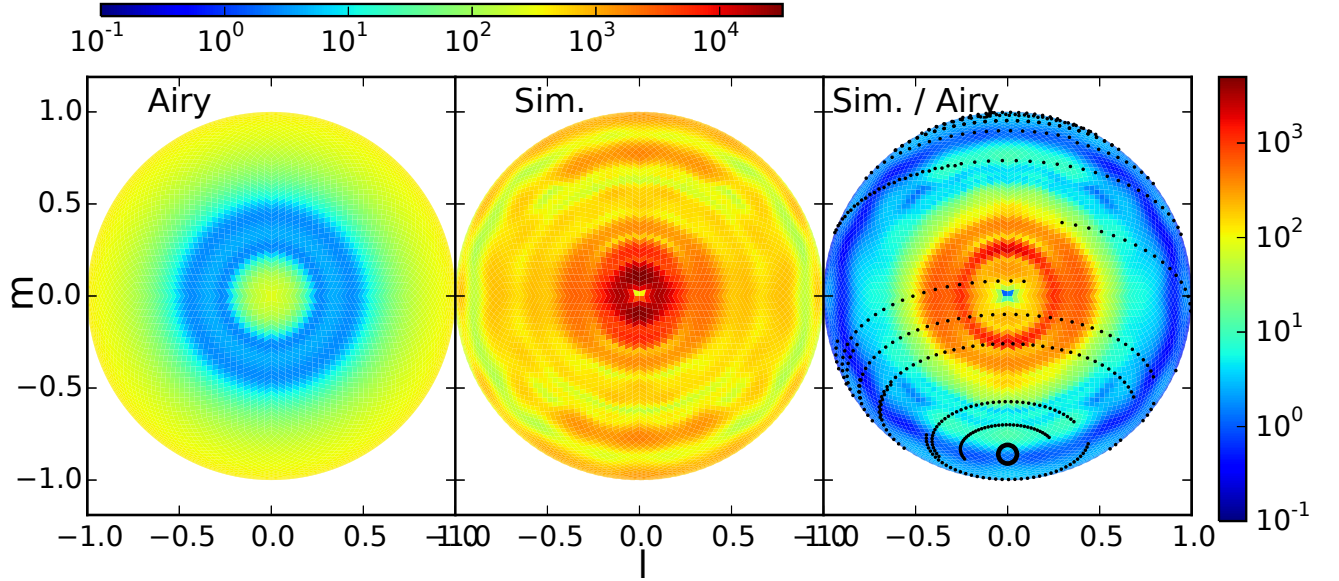


Figure 2. All-sky directional chromaticity of antenna power pattern.

foreground avoidance strategy, Fig. 4 shows delay spectra after applying a *Blackman-Harris* window function extending 10 MHz on each side centered on 150 MHz with effective bandwidth of 10 MHz. The 8 panels correspond to those shown in Fig. 3. As a result of narrowed subband, the resolution in delay space (and k_{\parallel}) has coarsened. The cyan and gray lines denote power spectra of EoR models 1 and 2 respectively.

Firstly, it is noted that the coarsening of delay resolution significantly absorbs the distinct differences caused by beams of different chromaticities as seen in the full band foreground delay spectra outside the *foreground wedge* in Fig. 3. Secondly, it is also found that barring the shortest baselines ($|b| \leq 29.2$ m), which have the most severe foreground contamination especially from diffuse emission, foreground contamination on baselines longer than $\gtrsim 29.2$ m is lesser than EoR signal power for $|k_{\parallel}| \gtrsim 0.22 h \text{ Mpc}^{-1}$ in either of the models.

Fig. 5 is similar to Fig. 4 except it is obtained with a subband *Blackman-Harris* window function centered on 170 MHz. In this subband relative to that centered on 150 MHz, the ratio of powers of the EoR signal and foregrounds is even higher outside the wedge thus indicating a stronger potential for direct detectability without the use of optimal power spectrum estimation techniques on almost all baseline lengths.

It must be emphasized that these are obtained only with windowing techniques and do not represent the best sensitivity achievable with sophisticated tools such as optimal covariance-based weighting schemes (Liu et al. 2014a,b; Ali et al. 2015; Dillon et al. 2015). Thus assuming the data is limited by foregrounds and not by thermal noise, this demonstrates that even with no sophistication in power spectrum estimation, a direct detection based on simple windowing and delay spectrum technique is possible on a majority of HERA baselines and will further allow distinguishing between different EoR models. This finding holds even in the most conservative scenario where the modeled beam pattern with most severe chromaticity inherently results in significant

and inherent foreground contamination outside the *foreground wedge*.

5.3. Constraints on Reflections between Antennas

Patra et al. 2015 (submitted) and Ewall-Wice et al. 2015 (submitted) discuss the measured and simulated reflections between a dish and its feed. We provide a related discussion by estimating the attenuation in power required to keep the foreground power reflected between adjacent antennas below the expected EoR HI signal level for the different models of power patterns used in our study.

The effect of reflections is to shift the measured foreground power to higher modes in τ (or equivalently in k_{\parallel}) and thus cause further contamination in these higher k_{\parallel} modes which are considered sensitive for EoR HI signal detection. Here we estimate the attenuation required at specific k_{\parallel} modes of interest to contain reflected foreground power between antennas below expected EoR HI power, both corresponding to a 14.6 m antenna spacing.

We define the required attenuation as the ratio:

$$\Gamma_{k_{\parallel}}(\tau) = \frac{P_{\text{HI}}(k_{\parallel})}{P_{\text{FG}}(k_{\parallel} - \frac{dk_{\parallel}}{d\tau} \tau)}, \quad (10)$$

where, $P_{\text{HI}}(k_{\parallel})$ is the EoR HI power spectrum for the chosen antenna spacing, $P_{\text{FG}}(k_{\parallel})$ is the foreground delay power spectrum obtained with a Blackman-Harris window function applied over the full band of the three uniquely oriented 14.6 m antenna spacings further averaged over a 0–12 hr LST range and over both positive and negative k_{\parallel} modes, τ is the delay caused by reflections, and $dk_{\parallel}/d\tau$ is the *jacobian* in the transformation of τ to k_{\parallel} .

Fig. 6 shows $\Gamma_{k_{\parallel}}(\tau)$ (in dB) for selected k_{\parallel} at $0.08 h \text{ Mpc}^{-1}$ (left), $0.1 h \text{ Mpc}^{-1}$ (middle), and $0.12 h \text{ Mpc}^{-1}$ (right) as a function of delays due to reflections from other antenna spacings. The light, medium and dark shaded curves show $\Gamma_{k_{\parallel}}(\tau)$ for achromatic, *Airy*, and chromatic antenna power patterns respectively.

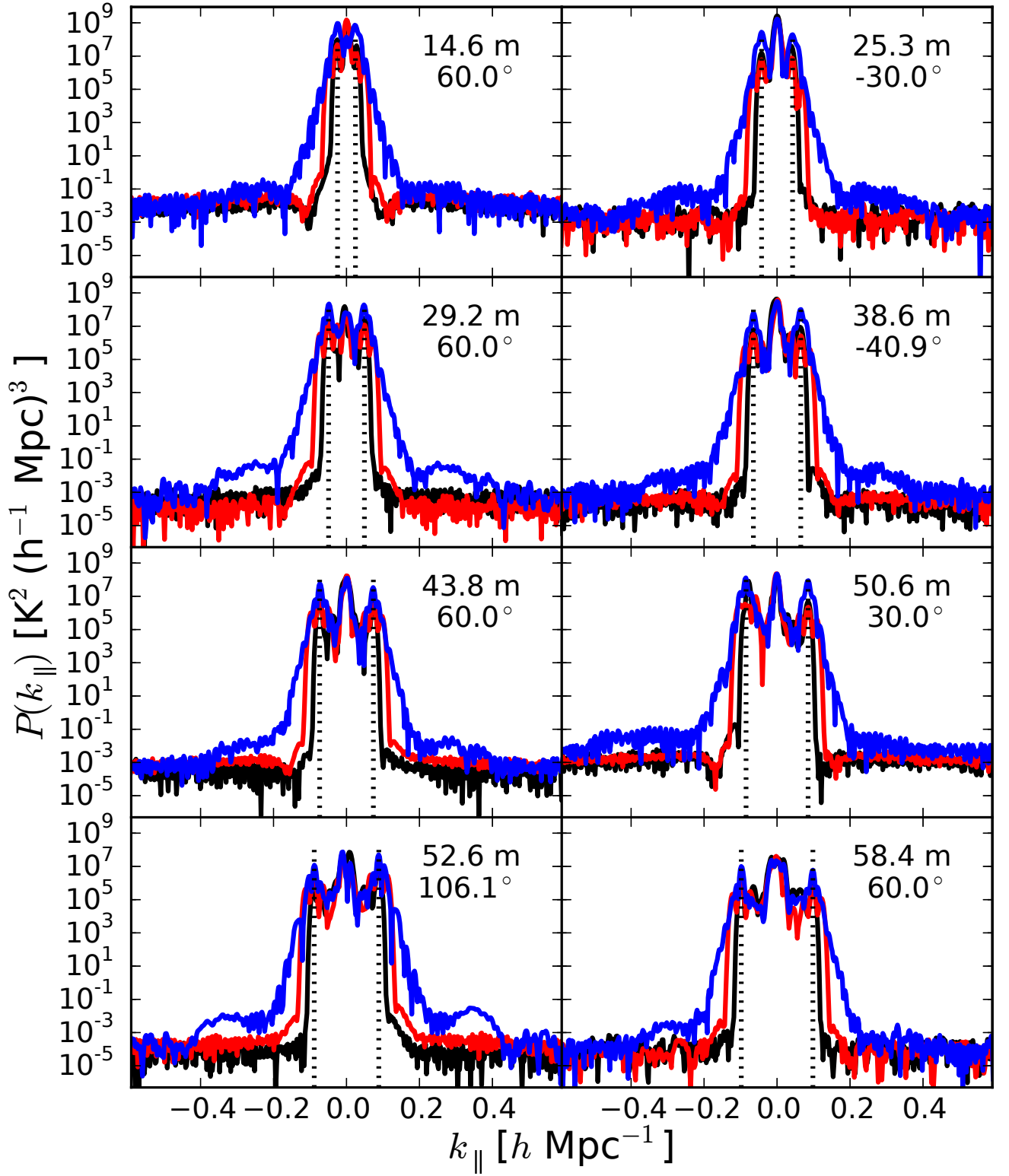


Figure 3. Effect of chromaticity of antenna power pattern on foreground delay power spectra for different baselines.

These curves set an upper limit to the reflected foreground power below the EoR HI signal power as a function of delays caused by antenna-to-antenna reflections. It is noted that a chromatic simulated power pattern sets the most severe upper limit in all three chosen k_{\parallel} for delays $\tau < 80$ ns (left), $\tau < 120$ ns (middle), and $\tau < 160$ ns.

The required attenuation is also a sensitive function of the chosen k_{\parallel} mode. For instance, at $k_{\parallel} = 0.08 h \text{ Mpc}^{-1}$, the reflections with delays 70 ns require to be attenuated by at $\gtrsim 85$ dB for the simulated power pattern, $\gtrsim 82$ dB for the *Airy* pattern, and $\gtrsim 70$ dB for the achromatic pattern. However, at $k_{\parallel} = 0.1 h \text{ Mpc}^{-1}$ for the same delay of reflection, the requirement on attenuation is lowered to $\gtrsim 75$ dB, $\gtrsim 30$ dB and $\gtrsim 22$ dB respectively. If the chosen k_{\parallel} is instead $0.12 h \text{ Mpc}^{-1}$, the required attenuation is further relaxed to $\gtrsim 60$ dB, $\gtrsim 15$ dB and $\gtrsim 15$ dB respectively. This further reinforces the significance of reducing the chromaticity of the antenna power pattern to further relax the constraint on the system to achieve the attenuation required to contain the reflected foreground power from other antennas from contaminating the sensitive EoR HI signal modes in the *EoR window*.

6. SUMMARY

This work was supported by the U. S. National Science Foundation (NSF) through award AST-1109257. DCJ is supported by an NSF Astronomy and Astrophysics Postdoctoral Fellowship under award AST-1401708. JCP is supported by an NSF Astronomy and Astrophysics Fellowship under award AST-1302774.

REFERENCES

- Ali, S. S., Bharadwaj, S., & Chengalur, J. N. 2008, MNRAS, 385, 2166
- Ali, Z. S., Parsons, A. R., Zheng, H., et al. 2015, ApJ, 809, 61
- Beardsley, A. P., Hazelton, B. J., Morales, M. F., et al. 2013, MNRAS, 429, L5
- Bernardi, G., de Bruyn, A. G., Brentjens, M. A., et al. 2009, A&A, 500, 965
- Bernardi, G., de Bruyn, A. G., Harker, G., et al. 2010, A&A, 522, A67
- Bock, D. C.-J., Large, M. I., & Sadler, E. M. 1999, AJ, 117, 1578
- Bowman, J. D., Morales, M. F., & Hewitt, J. N. 2009, ApJ, 695, 183
- Bowman, J. D., Cairns, I., Kaplan, D. L., et al. 2013, PASA, 30, 31
- Condon, J. J., Cotton, W. D., Greisen, E. W., et al. 1998, AJ, 115, 1693
- Datta, A., Bowman, J. D., & Carilli, C. L. 2010, ApJ, 724, 526
- de Oliveira-Costa, A., Tegmark, M., Gaensler, B. M., et al. 2008, MNRAS, 388, 247
- Di Matteo, T., Perna, R., Abel, T., & Rees, M. J. 2002, ApJ, 564, 576
- Dillon, J. S., Liu, A., & Tegmark, M. 2013, Phys. Rev. D, 87, 043005
- Dillon, J. S., Liu, A., Williams, C. L., et al. 2014, Phys. Rev. D, 89, 023002
- Dillon, J. S., Neben, A. R., Hewitt, J. N., et al. 2015, ArXiv e-prints, arXiv:1506.01026
- Furlanetto, S. R., & Briggs, F. H. 2004, New A Rev., 48, 1039
- Furlanetto, S. R., Oh, S. P., & Briggs, F. H. 2006, Phys. Rep., 433, 181
- Furlanetto, S. R., Zaldarriaga, M., & Hernquist, L. 2004, ApJ, 613, 1
- Ghosh, A., Prasad, J., Bharadwaj, S., Ali, S. S., & Chengalur, J. N. 2012, MNRAS, 426, 3295
- Gleser, L., Nusser, A., & Benson, A. J. 2008, MNRAS, 391, 383
- Iliev, I. T., Shapiro, P. R., Ferrara, A., & Martel, H. 2002, ApJ, 572, L123
- Lidz, A., Zahn, O., McQuinn, M., Zaldarriaga, M., & Hernquist, L. 2008, ApJ, 680, 962
- Liu, A., Parsons, A. R., & Trott, C. M. 2014a, Phys. Rev. D, 90, 023018
- . 2014b, Phys. Rev. D, 90, 023019
- Liu, A., & Tegmark, M. 2011, Phys. Rev. D, 83, 103006
- Liu, A., Tegmark, M., Bowman, J., Hewitt, J., & Zaldarriaga, M. 2009, MNRAS, 398, 401
- Lonsdale, C. J., Cappallo, R. J., Morales, M. F., et al. 2009, IEEE Proceedings, 97, 1497
- Madau, P., Meiksin, A., & Rees, M. J. 1997, ApJ, 475, 429
- Mauch, T., Murphy, T., Buttery, H. J., et al. 2003, MNRAS, 342, 1117
- McQuinn, M., Zahn, O., Zaldarriaga, M., Hernquist, L., & Furlanetto, S. R. 2006, ApJ, 653, 815
- Mesinger, A., Furlanetto, S., & Cen, R. 2011, MNRAS, 411, 955
- Morales, M. F., Bowman, J. D., & Hewitt, J. N. 2006, ApJ, 648, 767
- Morales, M. F., Hazelton, B., Sullivan, I., & Beardsley, A. 2012, ApJ, 752, 137
- Morales, M. F., & Hewitt, J. 2004, ApJ, 615, 7
- Paciga, G., Albert, J. G., Bandura, K., et al. 2013, MNRAS, 433, 639
- Parsons, A., Pober, J., McQuinn, M., Jacobs, D., & Aguirre, J. 2012a, ApJ, 753, 81
- Parsons, A. R., & Backer, D. C. 2009, AJ, 138, 219
- Parsons, A. R., Pober, J. C., Aguirre, J. E., et al. 2012b, ApJ, 756, 165
- Parsons, A. R., Backer, D. C., Foster, G. S., et al. 2010, AJ, 139, 1468
- Parsons, A. R., Liu, A., Aguirre, J. E., et al. 2014, ApJ, 788, 106
- Pober, J. C., Parsons, A. R., Aguirre, J. E., et al. 2013, ApJ, 768, L36
- Santos, M. G., Cooray, A., & Knox, L. 2005, ApJ, 625, 575
- Scott, D., & Rees, M. J. 1990, MNRAS, 247, 510
- Sunyaev, R. A., & Zeldovich, Y. B. 1972, A&A, 20, 189
- Taylor, G. B., Carilli, C. L., & Perley, R. A., eds. 1999, Astronomical Society of the Pacific Conference Series, Vol. 180, Synthesis Imaging in Radio Astronomy II
- Thompson, A. R., Moran, J. M., & Swenson, Jr., G. W. 2001, Interferometry and Synthesis in Radio Astronomy, 2nd Edition (Wiley)
- Thyagarajan, N., Udaya Shankar, N., Subrahmanyan, R., et al. 2013, ApJ, 776, 6
- Thyagarajan, N., Jacobs, D. C., Bowman, J. D., et al. 2015a, ApJ, 807, L28
- . 2015b, ApJ, 804, 14
- Tingay, S. J., Goeke, R., Bowman, J. D., et al. 2013, PASA, 30, 7
- Tozzi, P., Madau, P., Meiksin, A., & Rees, M. J. 2000, ApJ, 528, 597
- Trott, C. M., Wayth, R. B., & Tingay, S. J. 2012, ApJ, 757, 101
- van Cittert, P. H. 1934, Physica, 1, 201
- van Haarlem, M. P., Wise, M. W., Gunst, A. W., et al. 2013, A&A, 556, A2
- Vedantham, H., Udaya Shankar, N., & Subrahmanyan, R. 2012, ApJ, 745, 176
- Wang, X., Tegmark, M., Santos, M. G., & Knox, L. 2006, ApJ, 650, 529
- Zaldarriaga, M., Furlanetto, S. R., & Hernquist, L. 2004, ApJ, 608, 622
- Zernike, F. 1938, Physica, 5, 785

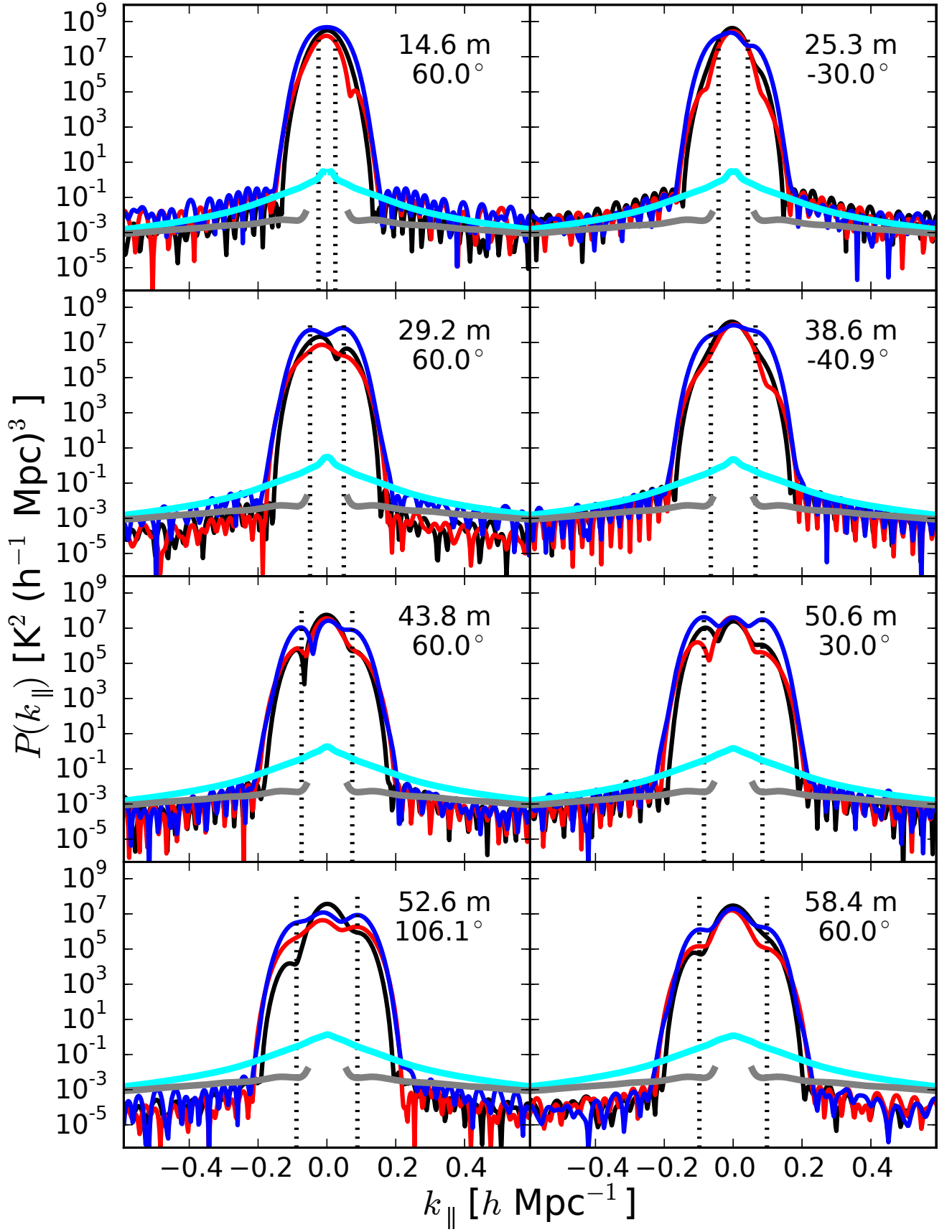


Figure 4. Effect of chromaticity of antenna power pattern on foreground delay power spectra obtained from the 150 MHz subband for different baseline lengths.

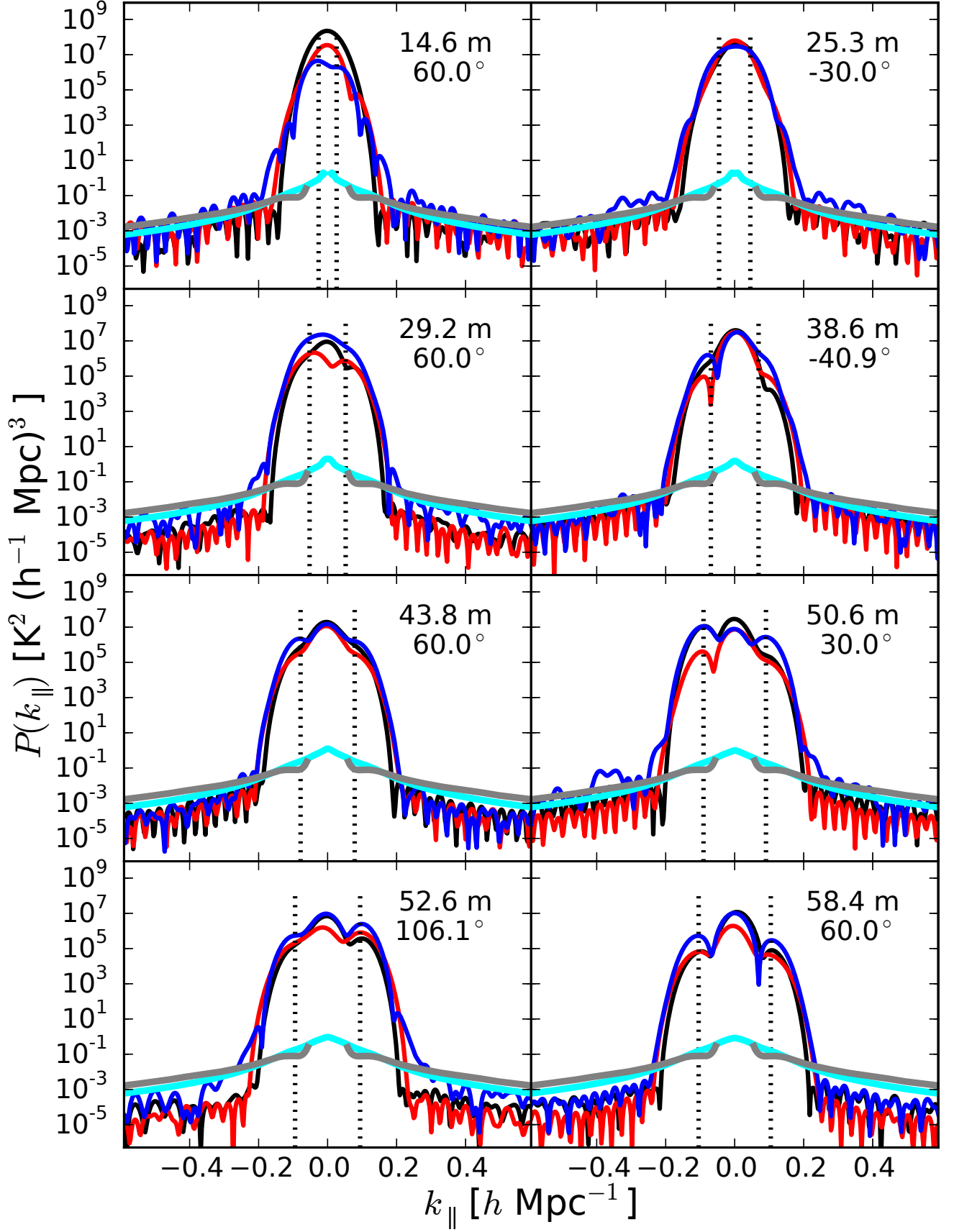


Figure 5. Effect of chromaticity of antenna power pattern on foreground delay power spectra obtained from the 170 MHz subband for different baseline lengths.

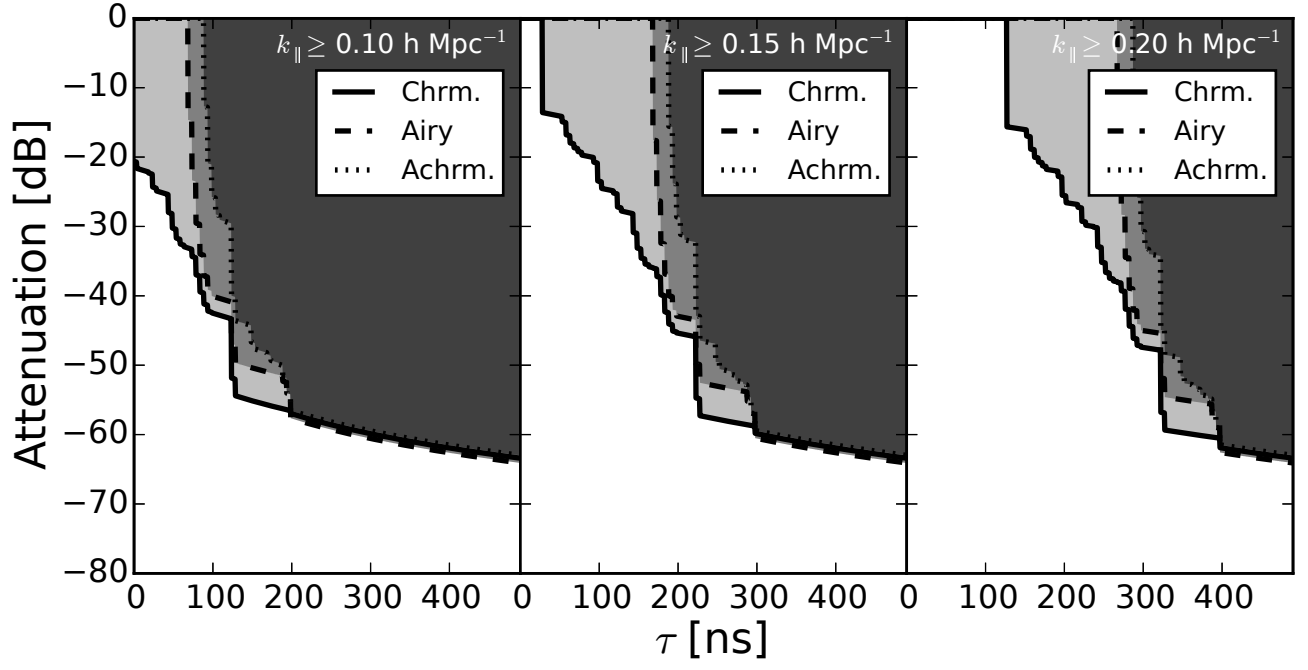


Figure 6. Attenuation of foreground power (in dB) from antenna-to-antenna reflections required to keep the reflected foreground power below EoR Hi signal power.